Journal of Molecular Spectroscopy **210,** 166–182 (2001)
doi:10.1006/jmsp.2001.8449, available online at http://www.idealibrary.com on IDEAL®

Wave Node Dynamics and Revival Symmetry in Quantum Rotors

William G. Harter

Department of Physics, University of Arkansas, Fayetteville, Arkansas 72701

E-mail: wharter@mail.uark.edu

Received July 24, 2001

Symmetries and dynamics of wave nodes in space and time expose principles of quantum theory and its relativistic underpinning. Among these are key principles behind recently discovered dephasing and rephasing phenomena known as *revivals*. A reexamination of basic Eberly revivals, Berry "quantum fractal" landscapes, and the "quantum carpets" of Schleich and co-workers reveals a simple Farey arithmetic and C_n-group revival structure in one of the earliest quantum wave models, the Bohr rotor. These principles may be useful for interpreting modern time-dependent rovibrational spectra. The nodal dynamics of the Bohr rotor is seen to have a quasi-fractal structure similar to that of earlier systems involving chaotic circle maps. The fractal structure is an overlay of discrete versions of Bohr's rotor model. Each N-point Bohr rotor acts like a base-N quantum "odometer" which performs rational fraction arithmetic. Such systems may have applications for optical information technology and quantum computing.

Wave phase behavior in space and time is fundamental to the understanding of physics and optics. Phase coherence has been an important idea since Huygens developed the principles of refraction in the late 1600s and it continues to be a basis of the quantum theory of atomic, molecular, or optical nanostructures. Newton's classical dynamics of the 1700s and the related Hamilton–Jacobi least-action principles of the 1800s were, in the mid-1900's, seen by Dirac and Feynman to result from the need for a stationary quantum phase. Only "right" paths which "agree" on an extremal phase value are able to win a kind of quantum lottery to exist while a vast majority of "wrong" paths cancel each other out in a cacophonous mishmash of mismatched phases.

Recently, the phenomena of *rephasing* or *revival* has arisen. Quantum revivals, like classical chaos and fractals, are a class of phenomena that many saw but few observed. Each has required modern computer simulations and graphics to make a convincing case for its existence, but each was thought, at first, to be an artifact of numerical code gone awry. Also, each of these phenomena is inadequately described by Newtonian differential continuum analysis but yields to discrete algebraic or number-theoretic approaches. Finally, revivals are relevant to a field entitled "quantum chaos," thought by some to be an oxymoron.

The term *revival* is a coinage by Eberly (*1*) to describe unexpected rephasing that appeared in 1976 computer studies of atom–quantum electrodynamics. For the next two decades there were sporadic reports of revival phenomena including *fractional revivals* in quantum treatments of simpler systems such as rotors (*2*), anharmonic vibrators (*3*), Rydberg orbitals (*4*), or an infinite square well or "particle-in-a-box" (*5*). A theory (*6*) of revivals in 1989 was based on box waves. Finally, in 1996 and 1997, Berry (*7*) and Schleich and co-workers (*8, 9*) used box wave simulations to plot "quantum fractal" landscapes and "quantum carpets" and thereby showed convincingly that revivals are a phenomenon whose theory and applications needs to be more deeply explored.

This work analyzes revival phenomena using symmetry group theory and a Farey arithmetic adapted from classical chaos theory. This new approach, which utilizes space–time behavior of wave phase-zeros or nodes, also suggests a kind of nanostructure that may be a base-N quantum computer of rational numbers. It also provides a wave-based derivation of special relativity that has extraordinary simplicity and clarity.

TWO-COMPONENT NODAL DYNAMICS

To introduce wave zero behavior in space–time, consider an interference of electromagnetic waves (photon or other mass-0 particle waves) such as is shown in Fig. 1a. Here a left-to-right-moving wave of amplitude $A_{\rightarrow} = 0.7$ collides with a right-to-left-moving wave of greater amplitude $A_{\leftarrow} = -0.9$. The result is a fixed wave envelope with standing wave ratio SWR of $valley : peak = (|A_{\leftarrow}| - |A_{\rightarrow}|)/(|A_{\leftarrow}| + |A_{\rightarrow}|) = -1 : 8$ for the wave magnitude $|\Psi| = \sqrt{\Psi * \Psi}$ which envelopes the real and imaginary parts $\mathrm{Re}(\Psi)$ and $\mathrm{Im}(\Psi)$. Inside $\pm|\Psi|$ is a "galloping" motion (*10*) of $\mathrm{Re}(\Psi)$ and $\mathrm{Im}(\Psi)$ which periodically exceeds and falls below the speed c of light by factors of SWR^{-1} and SWR. In the top frame of Fig. 1a, $\mathrm{Re}(\Psi)$ is a wave galloping at $-8c$ through a narrow opening of the envelope. Galloping motion is related to Kepler's law where orbiting particles slow at apogee and quicken at perigee (*10*).

Zeros of $\mathrm{Re}(\Psi)$ are open or solid dots which zigzag in the center space–time plot of Fig. 1a. First, $\mathrm{Re}(\Psi)$ shrinks to go

0022-2852/01 $35.00

through the SWR passage at 8 times the speed of light ($8c$) in about 1/9 of a period. Then it expands while coasting about 1/8 the speed of light ($c/8$) for a remaining 8/9 of a period. (Fig. 1a bottom) For exceeding the speed limit c of light, relativity theory mandates severe consequences: wave zeros undergo death by pair-annihilation followed by re-creation as described below by another observer. Wave zeros of positive slope are the solid green dots. Open red dots sit on zeros of negative slope which, tongue-in-cheek, are called "anti-zeros" below. The average phase velocity is that of light $c = \omega/k$, but super-c zigags become time switch-backs for a moving observer who, at velocity $u = -3c/5$, sees a Doppler blue-shift factor of 2.0 for left-to-right light and a red-shift factor of $1/2 = 0.5$ right-to-left light (Fig. 1b). Each speeding zero of Fig. 1a is seen by the moving observer (Fig. 1b) to be at three places at times between "zero-anti-zero" creation and annihilation. Zero-annihilation, creation, or both occur if a red and green dot meet because, at that moment, a Re(Ψ) minimum, maximum, or inflection point, respectively, crosses the x-axis.

If left and right amplitudes are made equal ($A_{\leftarrow} = A_{\rightarrow}$), as in Fig. 1c, the creation and annihilation events become simultaneous and all zero-velocities become uniform constant velocities according to the identity

$$\frac{1}{2}e^{i(k_{\rightarrow}x-\omega_{\rightarrow}t)} - \frac{1}{2}e^{i(k_{\leftarrow}x-\omega_{\leftarrow}t)} = ie^{i\frac{(k_{\rightarrow}+k_{\leftarrow})x-(\omega_{\rightarrow}+\omega_{\leftarrow})t}{2}} \sin\frac{(k_{\rightarrow}-k_{\leftarrow})x-(\omega_{\rightarrow}-\omega_{\leftarrow})t}{2}. \quad [1]$$

The exponential $e^{i\,\text{phase}}$ factor in [1] moves at a phase velocity

$$V_{\text{phase}} = \frac{\omega_{\rightarrow}+\omega_{\leftarrow}}{k_{\rightarrow}+k_{\leftarrow}}. \quad [2]$$

The sine factor moves at a group velocity

$$V_{\text{group}} = \frac{\omega_{\rightarrow}-\omega_{\leftarrow}}{k_{\rightarrow}-k_{\leftarrow}} = V_{\text{envelope}}. \quad [3]$$

For Fig. 1c the phase velocity is $V_{\text{phase}} = 5c/3$ by [2], and the group-envelope travels at $V_{\text{group}} = 3c/5$ by [3], which is consistent with speed $u = -3c/5$ of the observer relative to the (SWR = 8)-standing-wave envelope in Fig. 1a.

NODAL COORDINATES AND QUANTUM DISPERSION

If Fig. 1a were a *pure-standing* wave ($A_{\leftarrow} = A_{\rightarrow}$, SWR = 0) its zeros would trace a *square* space-time grid. Vertical ct-lines ($x = 0, \pm\pi, \pm 2\pi, \ldots$) are traced at 1/2-wave intervals by standing wave nodes. Horizontal x-lines ($ct = 0, \pm\pi, \pm 2\pi, \ldots$) appear at 1/2-period instants when Re(Ψ) is zero for all x, that is, when zeros go "infinitely fast." The diamond-shaped (x, ct) grid in Fig. 1c is the view by a ($u = -3c/5$)-moving (x', ct')-observer of a square (x, ct) grid. The (x, ct) lines are ($u = 3c/5$) Lorentz–Minkowski coordinates. As shown in Appendix A, this provides a simple wave-based derivation (*10*) of the relativistic Lorentz space-time coordinate transformation

$$x = (x' + (u/c)ct')/\sqrt{1-u^2/c^2} \quad [4a]$$

$$ct = ((u/c)x' + ct')/\sqrt{1-u^2/c^2}. \quad [4b]$$

This also leads to a wave-based derivation (*11*) of DeBroglie–Schrodinger quantum mechanics by relativistic symmetry arguments. We sketch these arguments here. To simulate the velocity u of a photon or particle distribution one boosts an observer to velocity-u and deduces the matter-wave dispersion function $\omega(k)$. For mass-0 photons, the frequency–wavevector dispersion relation is linear: $\omega = ck$ since $c = \omega/k$ is the only possible $M = 0$ phase velocity. For mass-M particles at rest, the Planck energy–frequency $E' = \hbar\omega'$ has a constant *non*-zero rest-frame value $\hbar\omega' = \hbar\mu$ for zero wave vector ($k' = 0$). The k and ω seen by an observer boosted to arbitrary velocity u are derived in Appendix B and in the next equation below. The Einstein rest-energy constant $\hbar\mu = Mc^2$ is derived in Appendix C.

Wave phase ($kx - \omega t$) for an *in vacuo* matter wave of any mass M is postulated to be a Lorentz invariant: $(kx - \omega t) = (k'x' - \omega' t')$. So the wavevector–frequency pair $(k, \omega/c)$ or (ck, ω) transforms like space–time (x, ct) and has an invariant analogous to $(x^2 - c^2t^2) = (x'^2 - c^2t'^2)$ for space-time:

$$(c^2k^2 - \omega^2) = (c^2k'^2 - \omega'^2) = (0 - (Mc^2/\hbar)^2). \quad [5a]$$

Another invariant gives the desired dispersion $\omega(k)$:

$$\omega^2 = \sqrt{[(Mc^2/\hbar)^2 + (ck)^2]}. \quad [5b]$$

Figure 2a shows a hyperbolic mass-M dispersion function $\omega(k)$. Its asymptote is a "light cone" for $M = 0$ photons.

Finally, Planck's postulate relates frequency to energy, $E = \hbar\omega$. The DeBroglie momentum relation $p = \hbar k$ seen by a moving observer follows if Planck's relation $E = \hbar\omega$ is true in all frames. Rest-frame momentum–energy $(cp', E') = (0, Mc^2) = (c\hbar k', \hbar\omega')$ Lorentz transforms by [4] into $(cp, E) = (c\hbar k, \hbar\omega)$ (see Appendix C):

$$p = \hbar k = Mu/\sqrt{1-u^2/c^2} \underset{u\to 0}{\longrightarrow} Mu. \quad [5c]$$

$$E = \hbar\omega = Mc^2/\sqrt{1-u^2/c^2} \underset{u\to 0}{\longrightarrow} Mc^2 + \frac{1}{2}Mu^2. \quad [5d]$$

At low speed $u \ll c$, Newtonian momentum Mu and KE $Mu^2/2$ emerge (Fig. 2b). The group velocity [3] emerges as the classical "particle" speed since its value u is opposite to -u of the observer relative to the $k' = 0$ rest-wave:

$$V_{\text{group}} = \frac{d\omega}{dk} = \frac{dE}{dp} = \frac{c^2p}{E} = \frac{c^2Mu/\sqrt{1-u^2/c^2}}{Mc^2/\sqrt{1-u^2/c^2}} = u. \quad [6a]$$

The wave phase velocity [2] is the inverse c^2/u of u (in units of c)

and faster than c as happens in Fig. 1c:

$$V_{\text{phase}} = \frac{\omega}{k} = \frac{c^2}{u} = \frac{c^2}{V_{\text{group}}}. \quad [6b]$$

MULTICOMPONENT NODAL DYNAMICS: REVIVALS

Extending the preceding two-frequency-component wave-node analysis to many Fourier components requires simplification. Wave-zeros of $\text{Re}(\Psi)$ are very complex for many ω values, so we plot zeros of magnitude $|\Psi|$ instead, as in Schleich's quantum carpets (*8, 9*) and Berry's quantum fractal landscapes (*7*). Figure 3 is space–time plots of multicomponent $|\Psi|$ similar to Figs. 1a–1c, but the $|\Psi|$ zeros or low-$|\Psi|$ regions are plotted in white or light shading. This is a difference between Fig. 3 and earlier plots of probability $|\Psi|^2$ which tend to emphasize wave peaks and show semiclassical particle trajectories. The plots in Fig. 3 do not show particle paths as well; instead, they tend to show zeros or where the particle is *not*.

Also, earlier work focused on a particle-in-a-box of width W, while the plots in Fig. 3 are for a Bohr rotor or a particle-on-a-ring of length L. The latter contains the former as a special case if $L = 2W$, and the extra freedom aids a group analysis done later. Here, the $u \ll c$ approximation in [5c] or Fig. 2b gives the energy dispersion spectrum $E = Mu^2/2 = p^2/2M$, where wavevector k_m or momentum p_m is quantized by ring-L boundary conditions: $p_m = \hbar k_m = \hbar 2\pi m/L = hm/L$. Here $m = 0, \pm1, \pm2, \pm3, \ldots$ are momentum quantum numbers and $h = 2\pi\hbar$:

$$E_m = (\hbar k_m)^2/2M = m^2(h)^2/2ML^2 = m^2 h\upsilon_1 = m^2\hbar\omega_1. \quad [7]$$

The fundamental Bohr frequency $\omega_1 = 2\pi\upsilon_1$ is the lowest transition frequency $\upsilon_1 = (E_1 - E_0)/h$. Finally, to amplify $|\Psi|$-zeros, the m-distribution is a zero-centered ($\bar{m} = 0$) Gaussian-weighted window function of 1/2-width Δm:

$$W_G(m) = e^{-[(|m|-\bar{m})/\Delta m]^2}. \quad [8a]$$

The resulting wave packet has the following space–time dependence:

$$\Psi(\phi, t) = \langle \phi, t \mid \Psi\rangle = \sum_{m=-\infty}^{\infty} W_G(m)\langle \phi, t \mid m\rangle\langle m \mid \phi_0\rangle$$

$$= \frac{1}{2\pi}\sum_{m=-\infty}^{\infty} W_G(m) e^{i(m\phi - m^2\omega_1 t)} e^{-im\phi_0}. \quad [8b]$$

The initial ($t = 0$) wave for centered momentum ($\bar{m} = 0$) and position ($\phi_0 = 0$) also becomes Gaussian for large Δm:

$$\Psi(\phi, 0) = \frac{1}{2\pi}\sum_{m=-\infty}^{\infty} e^{-m^2/\Delta m^2} e^{im\phi} \xrightarrow[\Delta m \gg 1]{} \frac{\Delta m}{2\sqrt{\pi}} e^{-\left(\frac{\Delta m}{2}\phi\right)^2}$$

$$= \frac{e^{-\left(\frac{\phi}{\Delta\phi}\right)^2}}{\Delta\phi\sqrt{\pi}}. \quad [8c]$$

The angular position–momentum uncertainty relation is $\Delta\phi \cdot \Delta m = 2 = \Delta x \cdot \Delta k$. Three space–time plots are given in Figs. 3a, 3b, and 3c, respectively, with decreasing momentum half-width $\Delta m = 9$, 3, and 1.5 and coarser spatial resolution $\Delta\phi/2\pi = 2\%, 6\%$, and 12%. Each is plotted for a full time period $\tau_1 = 1/\upsilon_1 = 2\pi/\omega_1$ after which it repeats. Figure 3a uses a fine spatial resolution $\Delta x \cdot = 0.02$ which requires 9-quantum excitation ($\Delta m = 9$). It shows a labyrinth of increasingly fine self-similar X-patterns or "Hofstadter braids" (*12*) seen in band problems involving chiral or Zeeman effects (*13*). In the second and third figures (3b and 3c), of lower excitation ($\Delta m = 3$, and 1.5, respectively), the finer X-patterns begin to disappear leaving one big X across Fig. 3c.

SEMICLASSICAL THEORY: FAREY SUMS AND QUANTUM SPEED LIMITS

Figure 3c provides a clue to the theory of revivals. Its X is like a zero crossing in the Lorentz grid in Fig. 1c, but with momentum values restricted by $\Delta m = 1.5$ to only the first two levels $m = 0$ and $m = \pm1$, so the only possible group (or phase) velocities according to [3] and [7] are $V_{\pm1} = \pm L/\tau_1$, a Bohr length L per Bohr time unit τ_1:

$$V_{\text{group}}^{\text{Bohr}}(m \leftrightarrow n) = \frac{\omega_m - \omega_n}{k_m - k_n} = \frac{(m^2 - n^2)h\upsilon_1}{(m-n)h/L}$$

$$= (m+n)\frac{L}{\tau_1} = (m+n)V_1. \quad [9]$$

The X in Fig. 3c has two zeros doing one lap in opposite directions around the Bohr ring in a Bohr period τ_1. The packet anti-nodes or "particles" do laps, too, but their paths are not contiguous like those of zeros or nodes since anti-node amplitudes fluctuate. (Anti-nodal revival peaks and phases are discussed later.) $|\Psi|$-nodes, being virtually dead, have an indestructibility not had by zeros of $\text{Re}\Psi$ which annihilate and re-create in Fig. 1b.

Relaxing the momentum uncertainty Δm allows more m-values and wave velocities: $\pm V_1, \pm 2V_1, \pm 3V_1, \ldots$, ranging up to $2\Delta m V_1$. By [9] the maximum lap rate or *quantum speed-limit* is $2\Delta m$, i.e., twice the maximum $|m|$. Each velocity gives a fractional lap time of $1/1, 1/2, 1/3, \ldots, 1/(2\Delta m)$ of the Bohr period. Such fractions are written in the margins of Fig. 3 and Fig. 4 at the point where a lap trajectory passes the point $\phi = \pm\pi$ opposite the origin $\phi = 0$ of the wave packet. An nth multiple n/D of an allowed fraction $1/D$ corresponds to the nth lap of a wave node ("zero") if D is odd or the nth lap of a wave anti-node ("particle") if D is even.

The n/D fractional lines in Fig. 4 highlight the wave paths in Fig. 3a. As excitation Δm increases, even-D "particle" paths begin to show up as well, as dark shadows in between the odd-D "zero" paths in Fig. 3a. Note a vertical zero-velocity path up the center and edge. Also seen in a high-Δm plot (Fig. 3a) are

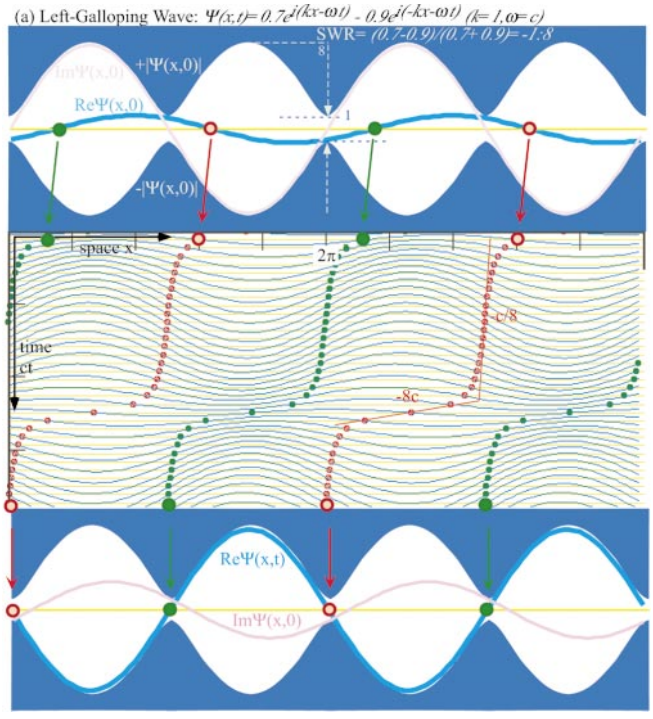

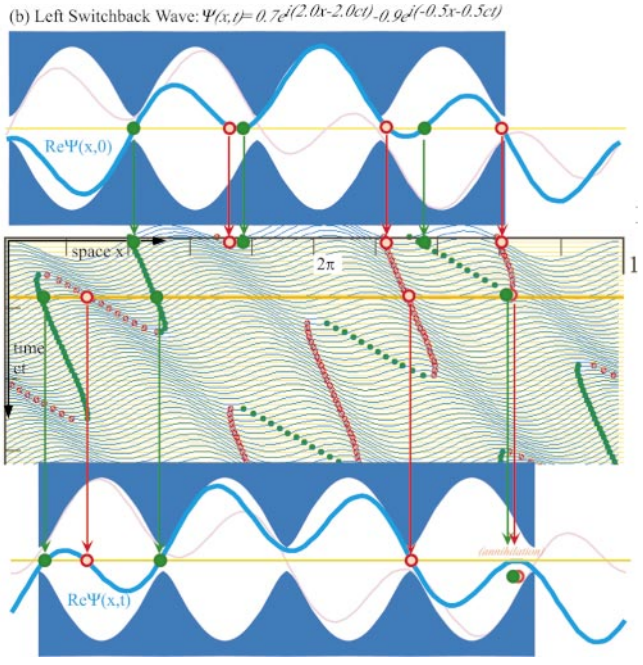

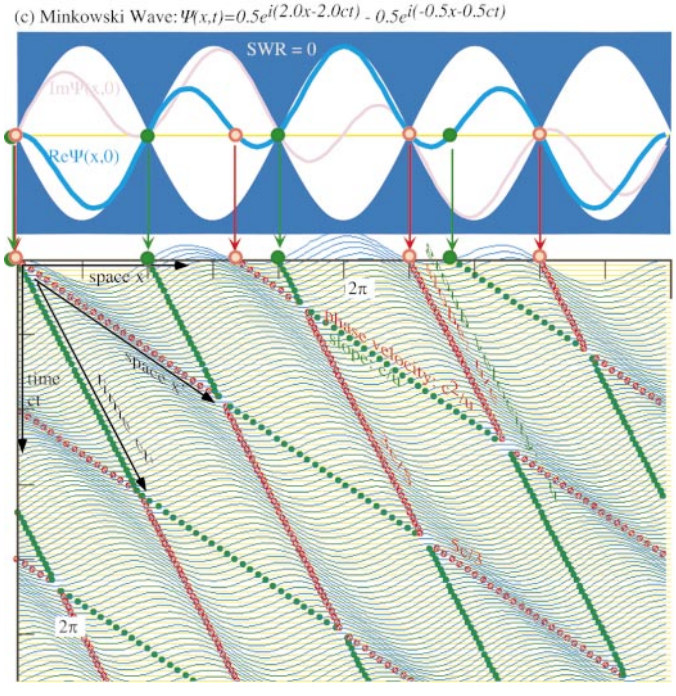

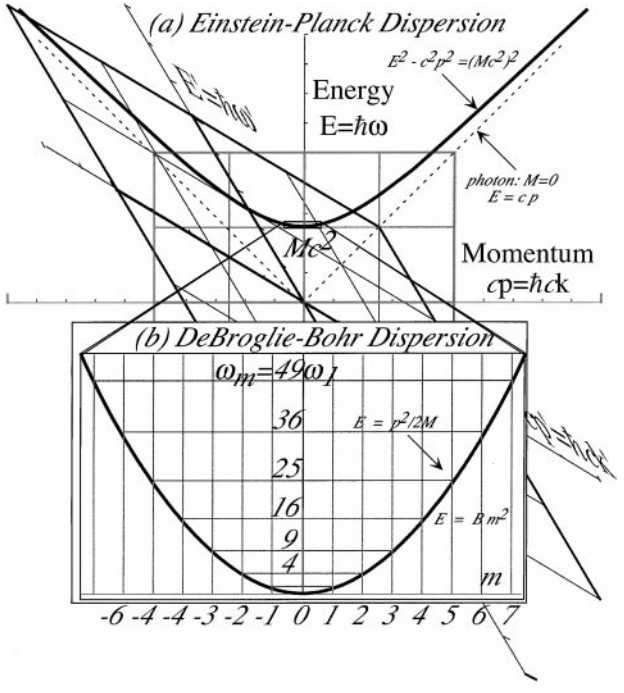

FIG. 1. Two-Fourier-component wave phase dynamics for counterpropagating waves. (a) Counterpropagating waves with the same wavevector k and frequency ω but differing amplitudes ($A_{\rightarrow} = 0.7$, $A_{\leftarrow} = 0.9$ give SWR $= 8$) exhibit a nonuniformly "galloping" phase velocity of zeros which ranges from $c/8$ to $8c$. (b) Counterpropagating waves with different (Doppler-shifted) wavevectors ($k_{\rightarrow} = 2k$, $k_{\leftarrow} = k/2$) and frequencies ($\omega_{\rightarrow} = 2\omega$, $\omega_{\leftarrow} = \omega/2$) and differing amplitudes (SWR $= 8$) exhibit creation and annihilation of zeros similar to what would be seen by an observer moving right to left at velocity $u = -3/5c$ relative to Fig. 1a. (c) Counterpropagating waves with different (Doppler-shifted) wavevectors ($k_{\rightarrow} = 2k$, $k_{\leftarrow} = k/2$) and frequencies ($\omega_{\rightarrow} = 2\omega$, $\omega_{\leftarrow} = \omega/2$) but the same amplitudes ($A_{\rightarrow} = 0.8 = A_{\leftarrow}$ give SWR $= \infty$) exhibit zeros making a $u = +3/5c$ Lorentz coordinate system relative to Fig. 1a. Lorentz ct-coordinate lines are zeros going at the wave group velocity $u = 3c/5$, while the Lorentz x-coordinate lines are zeros going at the wave phase velocity $u = 5c/3$.

FIG. 2. Vacuum electronic and photonic dispersion functions $\omega = \omega(k)$ or energy–momentum functions $E = E(p)$. (a) Exact relativistic dispersion $\omega = \sqrt{[(mc^2)2 + c^2k^2]}$. (b) Approximate (Newtonian) dispersion $E = mc^2 + p^2/2M$.

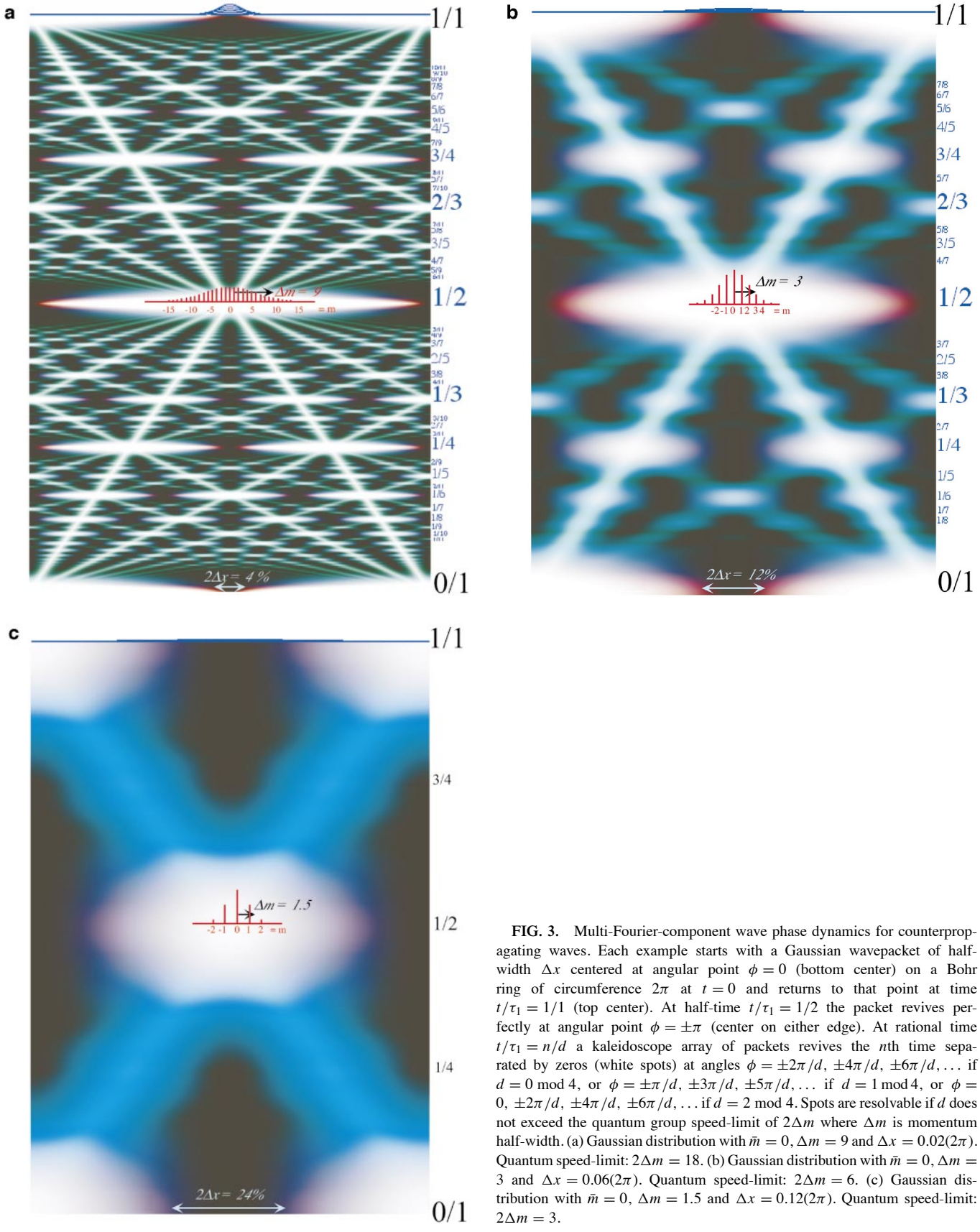

FIG. 3. Multi-Fourier-component wave phase dynamics for counterpropagating waves. Each example starts with a Gaussian wavepacket of half-width Δx centered at angular point $\phi = 0$ (bottom center) on a Bohr ring of circumference 2π at $t = 0$ and returns to that point at time $t/\tau_1 = 1/1$ (top center). At half-time $t/\tau_1 = 1/2$ the packet revives perfectly at angular point $\phi = \pm\pi$ (center on either edge). At rational time $t/\tau_1 = n/d$ a kaleidoscope array of packets revives the nth time separated by zeros (white spots) at angles $\phi = \pm 2\pi/d, \pm 4\pi/d, \pm 6\pi/d, \ldots$ if $d = 0 \bmod 4$, or $\phi = \pm\pi/d, \pm 3\pi/d, \pm 5\pi/d, \ldots$ if $d = 1 \bmod 4$, or $\phi = 0, \pm 2\pi/d, \pm 4\pi/d, \pm 6\pi/d, \ldots$ if $d = 2 \bmod 4$. Spots are resolvable if d does not exceed the quantum group speed-limit of $2\Delta m$ where Δm is momentum half-width. (a) Gaussian distribution with $\bar{m} = 0, \Delta m = 9$ and $\Delta x = 0.02(2\pi)$. Quantum speed-limit: $2\Delta m = 18$. (b) Gaussian distribution with $\bar{m} = 0, \Delta m = 3$ and $\Delta x = 0.06(2\pi)$. Quantum speed-limit: $2\Delta m = 6$. (c) Gaussian distribution with $\bar{m} = 0$, $\Delta m = 1.5$ and $\Delta x = 0.12(2\pi)$. Quantum speed-limit: $2\Delta m = 3$.

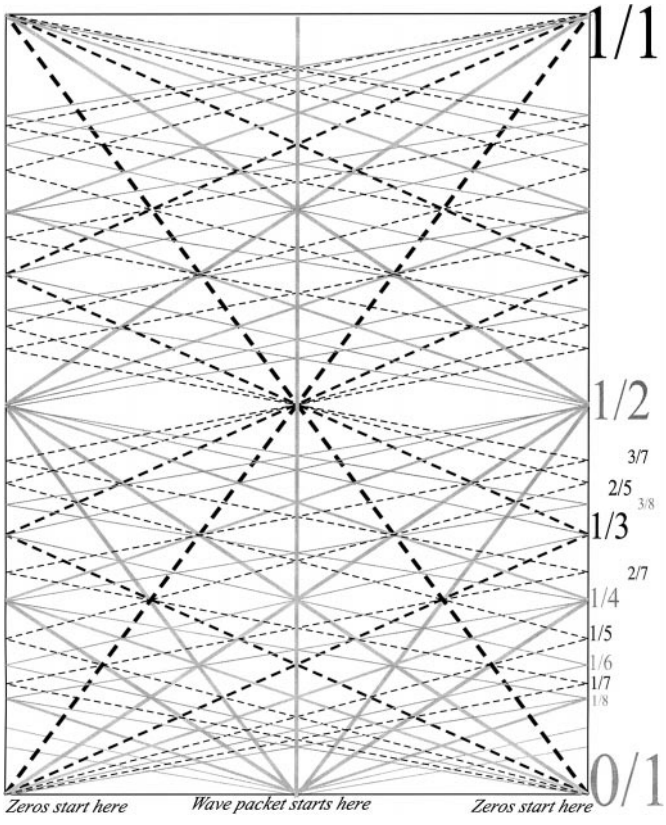

FIG. 4. Solid lines (anti-nodal or "particle" paths) and dashed lines (nodal or "zero" paths) correspond to dark and light paths, respectively, which make up X-paths in the wave space–time plots of Fig. 3.

"particle" pahts with odd *and* even fractional slopes emanating from the origin $\phi = 0$ of the wave packet.

The geometry of generic group velocity rays is sketched in Fig. 5 using two rays to form an asymmetric X around an intersection. (A symmetric X has equal group speeds d_1 and d_2.) Figure 3a is a patchwork of self-similar X patterns of nodal (odd-d_k) or anti-nodal (even-d_k) rays. The equations for the two lines in Fig. 5 are

$$\phi/2 = -d_1 t + n_1 + 1/2 \qquad \phi/2 = d_2 t - n_2 + 1/2. \quad [10a]$$

Subtracting the first ϕ equation from the second gives the intersection time for the center of the X:

$$t_{12-\text{intersection}} = \frac{n_2 + n_1}{d_2 + d_1} = \frac{n_2}{d_2} \oplus_F \frac{n_1}{d_1}. \quad [10b]$$

The resulting combination is called a *Farey sum* $\oplus_F$ of the rational fractions n_1/d_1 and n_2/d_2 after John Farey (*14*), an 1800s geologist. The Farey sum has been used to analyze classically "chaotic" or "fractal" structures (*15*), but its use in organizing quantum resonance structure is new. It begins with a fundamental Farey sum relating the beginning fraction (0/1) and ending fraction (1/1) of the fundamental ($0 \leftrightarrow 1$) resonance revival:

$$\frac{0}{1} \oplus_F \frac{1}{1} = \frac{1}{2}. \quad [11]$$

This is the instant $t/\tau_1 = 1/2$ for a half-time revival and the zero at the center of the fundamental X in Fig. 3c. The fundamental sum makes up the second row of a *Farey tree* (*16*) of such sums shown in Table 1. The sums in the Dth row of a Farey tree are an ordered set of all reduced fractions with denominator equal to D *or less*. We may terminate the tree at $D > 2\Delta m$ when denominator D exceeds the wave quantum speed limit $2\Delta m$ of [9]. Any finer revival peaks or zeros are unresolvable and more energy is needed to see such finer X structure.

The tracking of crests or wave peaks yields information about classical particle-like or group-wave motion. It is comforting to see familiar classical paths in what is often bewildering quantum cacophony but the clearest X-paths in Fig. 3a are *zeros* emanating from the point $\phi = \pm\pi$ where the particle packet originally was *not*. Quantum wave dynamics differs from classical dynamics is that multiple Fourier components easily interfere much of a wave to death. Most path phases lead to *non*existence except near (rare) stationary-phase paths which may be familiar classical ones. This is what is responsible for the particle localization that allows us to enjoy a Newtonian world and largely conceals its quantum wave nature from us. Where the wave is *not* provides important quantum clues. One recalls Sherlock Holmes' revelation that it is the "dog that did *not* bark" which solved a mystery.

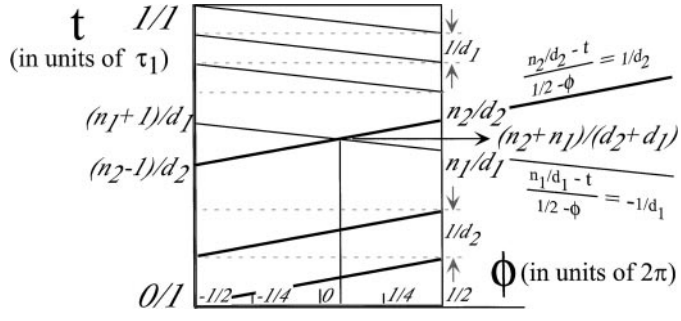

FIG. 5. Generic X-path intersection based on Farey sum always locates the position of a revival peak or zero.

C_2 QUANTUM THEORY: BASE-2 STATES

Motion of anti-nodal revivals for a 2-level excitation such as Fig. 3c are like beats of coupled pendulums (*17, 18*). Figure 6a shows *phasor* pictures of 2-cyclic (C_2) eigenstates. Phasor "clocks" are phase-space plots of $\mathrm{Re}\Psi$ vs. $\mathrm{Im}\Psi$ for the wavefunction $\Psi(p)$ at each spatial point $p = 0, 1$. $\mathrm{Re}\Psi$ is up, $\mathrm{Im}\Psi$ is to the left, and the area $\pi|\Psi|^2$ of the phasor is proportional to probability $|\Psi|^2$ at point p. Each eigenstate phasor rotates *clockwise* at its Bohr eigenfrequency $\omega_m = m^2\omega_1$; i.e., $\Psi(t) = e^{-i\omega_m t}\Psi(0)$. C_2 eigenstates are *even* $(0_2) = (+)$ or *odd*

TABLE 1
Farey Sum Tree

$D \le 1$	$\mathbf{\frac{0}{1}}$																										$\mathbf{\frac{1}{1}}$
$D \le 2$	$\frac{0}{1}$												$\mathbf{\frac{1}{2}}$														$\frac{1}{1}$
$D \le 3$	$\frac{0}{1}$							$\mathbf{\frac{1}{3}}$					$\frac{1}{2}$					$\mathbf{\frac{2}{3}}$								$\frac{1}{1}$
$D \le 4$	$\frac{0}{1}$						$\mathbf{\frac{1}{4}}$	$\frac{1}{3}$					$\frac{1}{2}$					$\frac{2}{3}$			$\mathbf{\frac{3}{4}}$					$\frac{1}{1}$
$D \le 5$	$\frac{0}{1}$				$\mathbf{\frac{1}{5}}$	$\frac{1}{4}$		$\frac{1}{3}$		$\mathbf{\frac{2}{5}}$			$\frac{1}{2}$			$\mathbf{\frac{3}{5}}$		$\frac{2}{3}$			$\frac{3}{4}$	$\mathbf{\frac{4}{5}}$				$\frac{1}{1}$
$D \le 6$	$\frac{0}{1}$			$\mathbf{\frac{1}{6}}$	$\frac{1}{5}$	$\frac{1}{4}$		$\frac{1}{3}$		$\frac{2}{5}$			$\frac{1}{2}$			$\frac{3}{5}$		$\frac{2}{3}$			$\frac{3}{4}$	$\frac{4}{5}$	$\mathbf{\frac{5}{6}}$			$\frac{1}{1}$
$D \le 7$	$\frac{0}{1}$		$\mathbf{\frac{1}{7}}$	$\frac{1}{6}$	$\frac{1}{5}$	$\frac{1}{4}$	$\mathbf{\frac{2}{7}}$	$\frac{1}{3}$		$\frac{2}{5}$	$\mathbf{\frac{3}{7}}$		$\frac{1}{2}$	$\mathbf{\frac{4}{7}}$		$\frac{3}{5}$		$\frac{2}{3}$	$\mathbf{\frac{5}{7}}$		$\frac{3}{4}$	$\frac{4}{5}$	$\frac{5}{6}$	$\mathbf{\frac{6}{7}}$		$\frac{1}{1}$
$D \le 8$	$\frac{0}{1}$	$\mathbf{\frac{1}{8}}$	$\frac{1}{7}$	$\frac{1}{6}$	$\frac{1}{5}$	$\frac{1}{4}$	$\frac{2}{7}$	$\frac{1}{3}$	$\mathbf{\frac{3}{8}}$	$\frac{2}{5}$	$\frac{3}{7}$		$\frac{1}{2}$	$\frac{4}{7}$		$\frac{3}{5}$	$\mathbf{\frac{5}{8}}$	$\frac{2}{3}$	$\frac{5}{7}$		$\frac{3}{4}$	$\frac{4}{5}$	$\frac{5}{6}$	$\frac{6}{7}$	$\mathbf{\frac{7}{8}}$	$\frac{1}{1}$

Note. Row-D accumulates all reduced rational fractions $n/d < 1$ with denominator d less than or equal to D. It also lists the resolvable revivals with quantum excitation index $(2\Delta m)$ less than or equal to D.

$(1_2) = (-)$ parity:

$$|+\rangle = |0_2\rangle = (|x\rangle + |y\rangle)/\sqrt{2} \qquad [12a]$$

$$|-\rangle = |1_2\rangle = (|x\rangle - |y\rangle)/\sqrt{2}. \qquad [12b]$$

$|m_2\rangle$ eigenfrequencies ω_m are $\omega_0 = 0$ and $\omega_1 = h/(2ML^2)$ by (7). $|m_2\rangle$ are + or − combinations of a local oscillator base state labeled $|x\rangle = |r^0\rangle$ (localized at spatial point $p = 0$ or $\phi = 0$) and a "flipped" base state $|y\rangle = \mathbf{r}|x\rangle = |r^1\rangle$ (localized at point $p = 1$ or $\phi = \pi$). States $|+\rangle$ and $|-\rangle$ are also eigenstates of C_2 "flip" operator $\mathbf{r}$ defined by $\mathbf{r}|x\rangle = |y\rangle$ and $\mathbf{r}|y\rangle = |x\rangle$, that is, $\mathbf{r}|+\rangle = +|+\rangle$, and $\mathbf{r}|-\rangle = -|-\rangle$. States $|+\rangle$ and $|-\rangle$ are analogous to "slow" (+45°) and "fast" (−45°) optical plane polarization eigenstates, respectively (*17*).

An initial 50–50 combination of the $|+\rangle$ and $|-\rangle$ eigenstates briefly recovers the first local base state $|x\rangle = (|+\rangle + |-\rangle)/\sqrt{2}$ lying between $|+\rangle$ and $|-\rangle$ in Fig. 6b. Since the $|-\rangle$-eigenstate is faster than the $|+\rangle$-eigenstate, the $|x\rangle$-state "beats" or *dephases* periodically. At 1/4 of a beat period τ_1, the fast $|-\rangle$ phase is 90° ahead (clockwise is $-i$) of the slow $|+\rangle$ giving a state $|L\rangle = (|+\rangle - i|-\rangle)/\sqrt{2}$ shown in Fig. 6b by two phasors of phase ±45°. This is analogous to optical 1/4-wave plates giving left-circular polarization. Then the fast eigenstate goes 180° ahead to give the "flipped" local base state of y-polarization $|y\rangle = (|+\rangle - |-\rangle)/\sqrt{2}$ in an optical analogy to action of 1/2-wave plates. Still later is the right circular state $|R\rangle = (|+\rangle + i|-\rangle)/\sqrt{2}$ (Fig. 6b bottom). Finally, at time $(1/1)\tau_1$ the initial $|x\rangle$ state (top of Fig. 6b) would reappear beneath Fig. 6b to repeat the revival sequence. In Fig. 6b, dotted lines making an X are drawn around the phasors to connect places where wave amplitude is low as on the X-pattern in Fig. 3c or at zeros in Fig. 1c. Low m-uncertainty ($\Delta m = 1.5$) means the revival wave is mostly a combination of the first *two* Bohr eigenlevels $m = 0$ and $|m| = 1$ having just two group (or phase) velocities $+V_1$ and $-V_1$.

C_N QUANTUM THEORY: BASE-N STATES

By considering discrete wave states it is possible to divide and conquer the continuous Bohr rotor wave spectral dynamics. The preceding C_2 treatment is analogous to the symmetry analysis of a diatomic rotor or a pair of quantum dots. Now the analysis is extended to that of the symmetry C_N of homocyclic molecules or polygonal arrangements of identical quantum dots as sketched in Fig. 7.

Understanding X-zero patterns and revivals at Farey level $D = 3$ involves a base-3 basis $\{|0_3\rangle|1_3\rangle|2_3\rangle\}$ of C_3. The bra state vectors $\{\langle 0_3|\langle 1_3|\langle 2_3|\}$ are drawn in Fig. 8a The C_3 wave states have quantized momentum $m = 0$, 1, and 2 modulo 3. $\langle 1_3|$ and $\langle 2_3|$ waves are like the Tesla 3-phase power transmission used today. Each m labels a row of three phasors in Fig. 8a which are like a discrete sampling of a wave in a Bohr level $m = 0$, 1, or 2.

In Fig. 8b are 4-*ary* C_4 base states of $m = 0$, 1, 2 and 3 modulo 4 quanta. In Fig. 9a are 5-*ary* C_5 base states of $m = 0, 1, 2, 3,$ and 4 modulo 5 quanta, and Fig. 9b has 6-*ary* C_6 bases of $m = 0$, 1, 2, 3, 4, and 5 modulo 6 quanta. These provide a basis for describing levels $D = 4$, 5, and $D = 6$ of the Farey tree. Each C_N system can also be thought of as a base-N counter. A binary C_2 system can count only to 2, that is, 0 to 1. A C_N system is capable of revivals that count from 0 to $N - 1$.

The C_N waves are bases of a finite and discrete Fourier analysis. Each C_N table in Fig. 7 (if all divided by $\sqrt{N}$) is an N-*by*-N unitary ($U(n)$) transformation matrix $\langle p \mid m\rangle$ of a *finite Fourier*

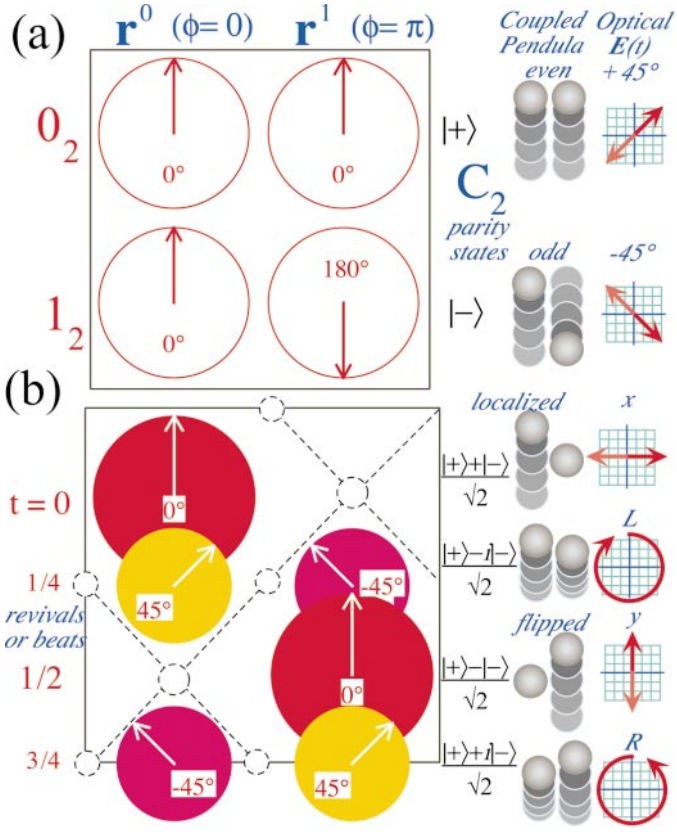

FIG. 6. The basic C_2-group and phase dynamics of a fundamental ($\Delta m = 1$) revival such as in Fig. 3c. (a) C_2-group characters $(0_2) = (1, 1)$ and $(1_2) = (1, -1)$ are plotted as complex phasors and related to even- and odd-parity eigenstates of a bilaterally symmetric coupled oscillator, pendulum system, or optical birefringent system. (b) Initially local state $(x) = (1, 0)$ is shown evolving through 1/4-fractional revival $(L) = (1 - i, i + i)/\sqrt{2}$ to 1/2-time revival $(y) = (0, 1)$ to 3/4-fractional revival $(R) = (1 + i, i - i)/\sqrt{2})$ on its way to a full revival of $(x) = (1, 0)$.

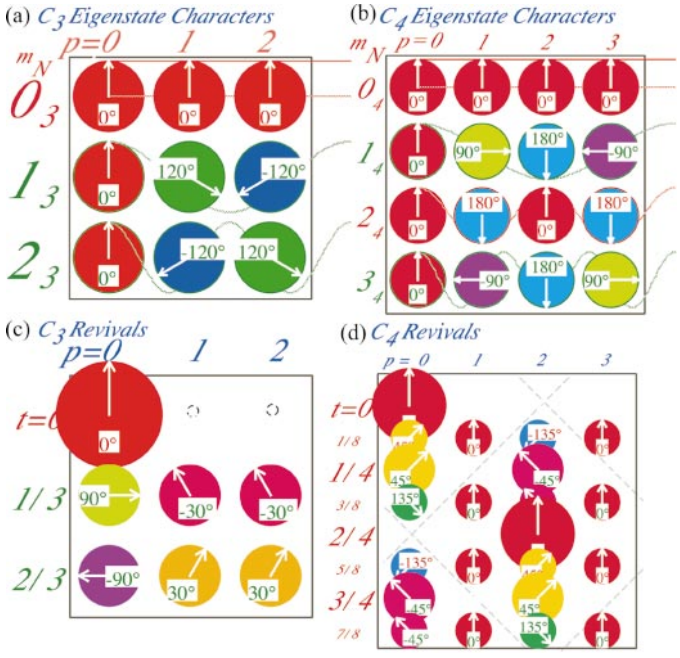

FIG. 8. The group character tables for (a) C_3 and (b) C_4 are analogous to the C_2 group character table in Fig. 6a. The group revival tables for (c) C_3 and (d) C_4 are analogous to the C_2 revival table in Fig. 6b. The C_2 group revival table is seen to be embedded in the revival table for C_4.

transform:

$$\langle p \mid (m)_N \rangle = \frac{e^{i(pm/2\pi N)}}{\sqrt{N}} = \langle (m)_N \mid p \rangle^* \quad (p, m = 0, 1, 2, \ldots, N-1). \quad [13]$$

Each phasor in Fig. 8 or 9 sits at one of N equally spaced lattice points $p = 0, 1, \ldots, N-1$ sketched in Fig. 7. Each phasor gives for a discrete angular point $p = 0, 1, 2, 3, \ldots, N-1$ the complex amplitude $\psi_{\pm m}(2\pi p/N) = \langle p \mid (m)_N \rangle = \langle (m)_N \mid p \rangle^*$ of a continuous running wave of a Bohr–Schrödinger eigenfunction $\psi_{\pm m}(\phi)$. A real (cosine) part of the eigenfunction is drawn for each eigenstate $|(m)_N\rangle$ in Figs. 8a, 8b and Figs. 9a, 9b to help connect it to the latter. The state notation $(m)_N$ labels these waves and may be read *m-modulo-N*, meaning that all waves having $m \pm nN$ wavelengths or quanta are an identical state $(m)_N$. (They are Fourier *aliases* $(m)_N = (m \pm nN)_N$.) In Fig. 7 each one of N equally spaced lattice points $p = 0, 1, 2, 3, \ldots, N-1$, is labeled by a pth power $\mathbf{r}^p$ of a fundamental C_N group rotation $\mathbf{r}$ by angle $2\pi/N$, that is, by $\mathbf{r}^0 = \mathbf{1}, \mathbf{r}^1, \mathbf{r}^2, \mathbf{r}^3, \ldots, \mathbf{r}^{N-1}, \mathbf{r}^N = \mathbf{1}$, respectively. This labeling notation simply lists the operator elements of the cyclic C_N symmetry group. The phasors are graphical representations of the complex eigenvalues or *characters* of the various cyclic groups. It should be noted that the binary C_2 phasor table (Fig. 6a) is embedded as a subset in the C_4 table of Fig. 8b since C_2 is a subgroup of C_4. C_2 is also seen in the C_6 table (Fig. 9b) or any C_N table of even-N since C_2 is a subgroup of all C_{2n}. The C_6 table also has the C_3 table (Fig. 8a) embedded. (C_n is a subgroup of C_m if m is divisible by n.) Subgroup embedding helps explain the fine details of revivals in Fig. 3 a. It also gives phase values that are not shown in Fig. 3.

C_N REVIVAL TABLES: BASE-N COUNTERS

For each subgroup embedding there is a corresponding embedding of the C_N *revival tables* shown in Figs. 8c, 8d and Figs. 9c, 9d, obtained, as in Fig. 6b, by first summing (times $1/\sqrt{N}$) all the rows of phasors in the character table C_3, C_4, C_5, or C_6 of Figs. 8a, 8b and Figs. 9a, 9b, respectively. This localizes 100% of the initial wave onto the first phasor position state $|x_0\rangle$:

$$|x_0(t=0)\rangle = \sum_{m=0}^{N-1} |(m)_N\rangle\langle (m)_N \mid x_0\rangle = \sum_{m=0}^{N-1} |(m)_N\rangle/\sqrt{N}. \quad [14]$$

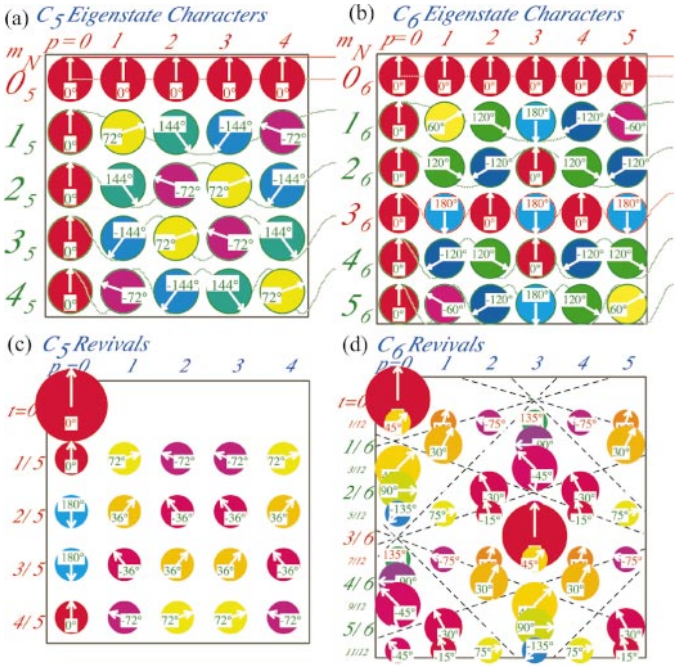

FIG. 9. The group character tables for (a) C_5 and (b) C_6 and revival tables for (c) C_5 and (d) C_6. The C_2 and C_3 revival table is seen to be embedded in the C_6 table. Relevant group velocity lines are drawn to help relate the tables to Figs. 3a, 3b, and 4.

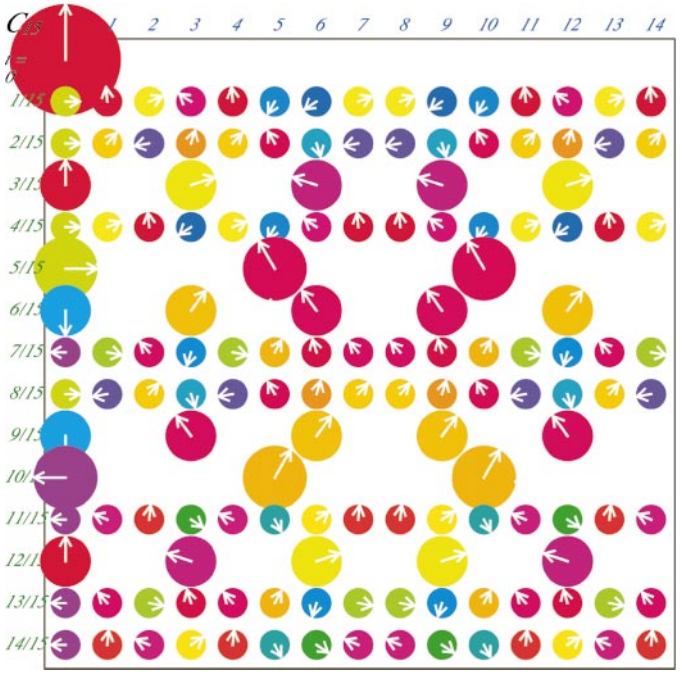

FIG. 10. The revival table for C_{15}. The C_3 and C_5 revival tables are seen to be embedded in the C_{15} table. The resulting zeros are indicators of the factors 3 and 5 of the integer $N = 15$.

Then each term $|(m)_N\rangle$ in the sum [14] is allowed to advance its phase $e^{-i\omega_m t} = e^{-im^2\omega_1 t}$ in discrete time fractions $1/N$ of a Bohr period τ_1 for *N-odd* or $1/2N$ of τ_1 for *N-even*, that is, through *stroboscopic instants* t_υ:

$$|x_0(t_\upsilon)\rangle = \sum_{m=0}^{N-1} e^{-im^2\omega_1 t_\upsilon} |(m)_N\rangle/\sqrt{N},$$

$$t_\upsilon = \begin{cases} \upsilon\frac{\tau_1}{N} = \frac{2\pi\,\upsilon}{\omega_1 N} & (\upsilon = 1, 2, \ldots, N-1) \qquad \text{for } N-\text{odd} \\ \upsilon\frac{\tau_1}{2N} = \frac{\pi\,\upsilon}{\omega_1 N} & (\upsilon = 1, 2, \ldots, 2N-1) \qquad \text{for } N-\text{even}. \end{cases} \quad [15]$$

For each stroboscopic instant or row in Figs. 8c, 8d or Figs. 9c, 9d there is an array of equally sized and equally spaced phasors, that is, a *kaleidoscopic* phasor array of revivals. At each t_υ, some phasors are revived, and the others, which lie between the revived ones, are zeroed out.

An even-$N = 2p$ revival table, such as $N = 4$ (Fig. 8b) or $N = 6$ (Fig. 9b), has embedded the $N = 2$ revival or "beat" table in Fig. 6b since C_2 is a C_{2p} subgroup. So it has a half-time 100% (single-peak) revival halfway around as well as 1/4-time and 3/4-time 50% (double-peak) revivals for $N = 2$ at each of the 1/4-lattice points, that is, for $N = 6$, at $t = 3/12$ and $t = 9/12$, and for $N = 4$, at $t = 2/8$ and $t = 6/8$. (τ_1 is the time unit being used here.)

An even-N revival table must start all over again at half-time but shifted by $\phi = \pi$ to a point halfway around the ring as required by C_N symmetry and by C_2 half-time 100% revival at the half-way point $p = N/2$. So the C_4 phasors below the $(p = 2, t = 2/4 = 1/2)$ point in Fig. 8d, namely, $t = 5/8$, $3/4$, and $7/8$, must have positions, amplitudes, and phases relative to the mid-point $p = 2$ that are identical to ones at $t = 1/8$, $1/4$, and $3/8$, respectively, below the initial $t = 0 = p$ point. Similar repetition is seen for $N = 6$ in Fig. 9d and for any *even-N* revival table below $t = 1/2$. Because $N = 6$ is also divisible by 3 there will be $N = 3$ revivals embedded at $t = 4/12 = 1/3$ and $t = 8/12 = 2/3$, and (relative to the 1/2-time revival) at $t = 1/3 - 1/2 = -1/6$ and $t = 1/3 + 1/2 = 5/6$ as well as at $t = 2/3 - 1/2 = 1/6$ and at $t = 2/3 + 1/2 = 7/6$. Phase angle "combinations" for each time are unique as in a kind of quantum "odometer."

Odd-prime-N revival tables (e.g., $N = 3$ in Fig. 8a) lack embedded structure. C_3 has only a subgroup C_1. Odd-prime-N revival tables have N phasors of area $1/N$ at each of $N - 1$ fractional revival times τ_1/N to $(N-1)\tau_1/N$. At $t = 0$ and $t = \tau_1$ a single area-1 phasor rises at $\phi = 0$. In contrast, even numbers such as $N = 4$ and 6 in Fig. 8d or 9d have revivals of area r/N for each subgroup $C_{N/r}$ of C_N, beginning with C_1 $(r = N)$ and C_2 $(r = N/2)$. (The only even-prime is $N = 2$.) For each factor r of N, there will be arrays of $N_r = N/r$ revival peaks and $N - N_r$ zeros which appear with the same times and phases seen in the revival table for the subgroup $C_{N/r} = C_{Nr}$. Phase varies with phasor position $\rho = 0, 1, 2, \ldots, N-1$ according

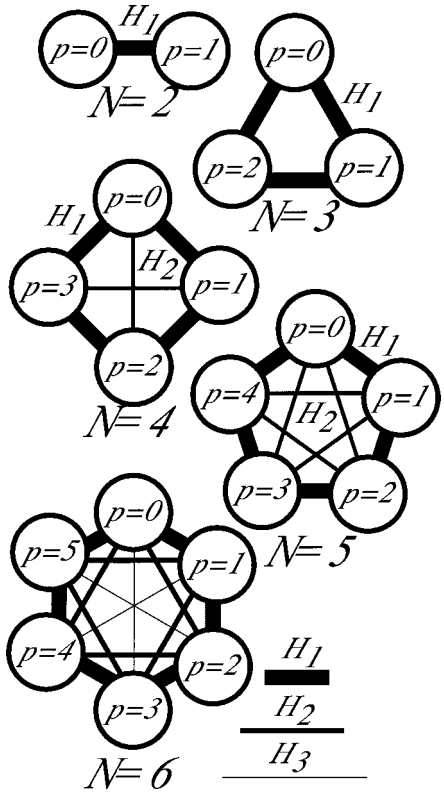

FIG. 7. Cyclic structures of C_2, C_3, C_4, C_5, and C_6 symmetry. Tunneling path amplitudes H_2, H_3, are sketched.

to $\rho^2 2\pi/N$. (This is shown in Ref. (*18*).) Hence phase appears nearly stationary around fundamental (single-peak) C_1 and C_2 revivals at $(\phi = 0, t = \tau_1)$ and $(\phi = \pi, t = \tau_1/2)$.

A given Δm-wavepacket evolution such as in Figs. 3a–3c may be characterized by an even integer nearest the quantum speed-limit $N \leq 2(\Delta m)$. Each peak of resulting revival structure is centered on a phasor in a revival table like Figs. 8d, 8c or Figs. 9d, 9c for a C_n in the sequence $C_N, C_{N-1}, C_{N-2}, \ldots, C_2$. Each revival peak shape is a similarly shaped "clone" of the initial Gaussian wavepacket and its peak phase and amplitude are those of its corresponding C_n phasor at that space-time location.

Revival pattern complexity grows rapidly with Δm and N as larger C_n groups are added to the high end of the sequence $C_N, C_{N-1}, C_{N-2}, \ldots, C_2$. Each increase in Δm by 1 means N increases by 2 and makes new $(N+1)$-peak and $(N+2)$-peak revivals resolvable to give $(N+1)^2$ and $(N+2)^2$ new peaks and zeros per unit space-time cell.

For $\Delta m = 1$ or $N = 2$ there are only the C_2 patterns of one- or two-peak revivals as seen in Fig. 3c or Fig. 6. C_2 patterns are also the largest and most clearly resolvable patterns for higher $\Delta m > 1$, as seen in Figs. 3a and 3b. Finer patterns with $2\Delta m \sim 4, 6, 8, 10, \ldots$ peaks belong to even $C_4, C_6, C_8, C_{10}, \ldots$ revival tables, respectively. Even-N peaks are interspersed with patterns of $\Delta m = 3, 5, 7, 9, \ldots$ peaks seen, respectively, in odd $C_3, C_5, C_7, C_9, \ldots$ revival tables.

To summarize, resolvable revival peaks and zeros for a given $N = 2(\Delta m)$ occur at time fractions given by the $D = N$ level of a Farey tree and are located and described by overlapping $C_N, C_{N-1}, C_{N-2}, \ldots, C_n$ revival tables. Subgroups C_n of any preceding $C_N, C_{N-1}, \ldots$ are embedded in the latter. For example, $\Delta \sim 3$ or $N \sim 6$ revivals happen at time fractions in the $D = 6$ row of the Farey tree. The $\Delta m \sim 3$ revival peak and zero structure plotted in Fig. 3b requires only C_6, C_5, and C_4 tables since C_3, C_2, and C_1 are subgroups of C_6 or C_4.

Because revivals expose C_N subgroups they can be made to find factors of an integer N. For C_m to be a subgroup of C_N, integer m must be a factor of N. Each revival table of Fig. 8d or 9d develops zeros at time row-$t = \nu/N$ if and only if ν and N share a common factor. The odd-$N = 3$ or 5 revivals in Fig. 8c or 9c have no zeros except in row $\nu = 1$ and row $\nu = N$ since these N are prime numbers which have no factors but 1 and N. For odd-N that is composite (nonprime) such as $N = 15$, the zeros show up on the atom or dot adjacent to the one on which the initial wave packet begins as shown in Fig. 10. The factors 3 and 5 of 15 are indicated by the $(p = 1)$-column zeros seen in rows $\nu = 3$ and $\nu = 5$, as well as $\nu = 6, 9, 10, 12$, and (of course) $15 = 0 \bmod 15$, for a C_{15} revival in Fig. 10.

REVIVAL TABLE COMBINATION: MULTIMODAL DISTRIBUTIONS

Cyclic C_N symmetry requires that a cyclic reordering of columns of a revival table, such as Fig. 10 or preceding examples, must also give a valid table. In other words, the phasor at origin $(p = 0)$ is only one of N points to start a revival packet. Furthermore, linearity requires that a linear combination of such tables be valid, as well. Vector addition of each phasor pair from a pair of two overlapping revival tables gives a valid multi-modal revival schedule. This explains how initial $\Psi(x, 0)$ packets have their starting shapes "cloned" at fractional revivals.

A zero-centered $(\bar{m} = 0)$ or mono-modal Gaussian (8a) evolves only by Δm-spreading. For $\bar{m} > 0$, the m-distribution (Fig. 11 top) and $\Psi(x, t)$ for $t > 0$ are bimodal as two Gaussian packets speed away from each other with group velocities of $\pm 2\bar{m}$ while spreading at a rate $2\Delta m$. A $(\bar{m} = 30, \Delta m = 5)$ space–time pattern in Fig. 10 has striated X-paths like Fig. 3c along the semiclassical paths of Fig. 4. But there is little distinction between zero-paths and particle paths; the former have a white (zero) center while the latter have a dark center.

Such bimodal evolution could be modeled discretely using overlapping $C_N, C_{N-1}, \ldots$ revival tables. It would be a crowded array of C_N phasors starting with $N = 2(\bar{m} + \Delta m) \sim 70$ and subgroups in a C_{70} sequence; with, perhaps, literally thousands of phasor plots. Clearly, a semiclassical description (*7–9*) is more immediately useful here. The purely quantum effects are reduced to faint striations and fuzz patches in Fig. 11. However, the fundamental quantum structure of the detailed evolution is no less existent just because it is out of sight.

CONCLUSION AND APPLICATIONS

The value of the C_N models increases when the purely quantum effects, particularly those of a *single* C_N, are to be isolated. One imagines having a discrete Bohr ring like those sketched, in Fig. 7 composed of N atoms, quantum dots, optical fibers, or Josephson circuits (*19*) homocyclically coupled is such a way that the usual quadratic Bohr dispersion spectrum $\omega_m = m^2\omega_1$ is obtained with a finite number N of states per band. As a first approximation, such a ring has a *Bloch* dispersion spectrum $\omega_m = (H_0 - 2H_1 \cos am)$ where H_1 is the nearest-neighbor coupling amplitude. Such a Bloch spectrum only approximates a Bohr spectrum for low m-values, and so high-Δm revivals would decay eventually. However, by inserting cross-connecting coupling paths $H_2, H_3, H_4, \ldots, H_{N/2}$, as shown in Fig. 7, it is possible to achieve any spectrum, including m^2, by adjusting coefficients H_k in a Fourier series:

$$\omega_m = H_0 - 2S_1 \cos am - 2H_2 \cos 2am - 2H_3 \cos 3am \ldots - H_{N/2} \cos Nam/2.$$

A quadratic spectrum ($E_m = h\upsilon m^2$) is achieved for general N by setting Hamiltonian parameters as follows:

$$h\upsilon m^2 = \sum_{p=0}^{N-1} H_p e^{-ipm\frac{2\pi}{N}}, \quad \text{where } H_p = \frac{h\upsilon}{N} \sum_{\{m\}} m^2 e^{ipm\frac{2\pi}{N}}. \qquad [16]$$

For example, a 4-level $N = 6$ quadratic spectrum $\{E_0 = 0, E_{\pm1} = 1^2 E_{\pm2} = 2^2, E_3 = 3^2\}$ involves six eigenstates, $|(m)_6\rangle = |(0)_6\rangle, |(\pm1)_6\rangle, |(\pm2)_6\rangle$, and $|(3)_6\rangle$, using the following coupling amplitudes as given in the $N = 6$ row of Table 2:

$$H_0 = 3.16, \quad H_1 = -2.0 = H_5^*, \quad H_2 = 0.67 = H_4^*, \quad H_3 = -0.5. \qquad [17]$$

With the adjustments in Table 2 of H_k coupling, pure C_N revivals like those in Figs. 8–10 would repeat at frequency $\upsilon = h^{-1}$ until the coupling was turned off. Such a device would be an N-ary counter as implied before. By incorporating the N-ring as the crossection of a coaxial N-fiber cable, it would be possible for the revival evolution to occur as an N-phase wave propagated down the cable. Write–read and reprogramming could be arranged along the length of the cable through varied intracoaxial coupling and intercoupling with other cables. The possibility of storing, processing, and transporting quantum or classical N-ary data for $N \gg 2$ using just one kind of basic hardware may yet warm the heart (and portfolio) of a future cyberentrepreneur.

APPENDIX A

Wave-Based Derivation of Relativistic Transformations

A moving optical wave source of frequency ω_0 such as an argon laser will be received with a Doppler blue-shifted frequency $\omega_1 = f\omega_0$ if it is approaching at velocity u. Relativistic symmetry requires that this frequency factor f be dependent only on the *relative* velocity u between transmitter and receiver. Furthermore, the relation $\omega_1 = f\omega_0$ must hold if time is reversed, so the relative velocity is reversed ($u \to -u$), as are the roles of transmitter and receiver. Thus a wave source of frequency ω_1 will be received at a Doppler red-shifted frequency $\omega_0 = \omega_1/f$ as the receiver–transmitter pair recede from each other at velocity $-u$.

This sets up the situations depicted in Fig. A.1. Two identical argon lasers point at each other in Fig. A.1a and produce a

TABLE 2
***N*-Discrete m^2-Hamiltonian Coupling Coefficients**

	H_0	H_1	H_2	H_3	H_4	H_5	H_6	H_7	H_8
$N = 2$	1/2	−1/2							
$N = 3$	2/3	−1/3							
$N = 4$	3/2	−1	1/2						
$N = 5$	2	−1.1708	0.1708						
$N = 6$	19/6	−2	2/3	−1/2					
$N = 7$	4	−2.393	0.51	−0.1171					
$N = 8$	11/2	−3.4142	1	−0.5858	1/2				
$N = 9$	20/3	−4.0165	0.9270	−1/3	0.0895				
$N = 10$	17/2	−5.2361	1.4472	−0.7639	0.5528	−1/2			
$N = 11$	10	−6.0442	1.4391	−0.5733	0.2510	−0.0726			
$N = 12$	73/6	−7.4641	2	−1	2/3	−0.5359	1/2		
$N = 13$	14	−8.4766	2.0500	−0.8511	0.4194	−0.2028	0.06116		
$N = 14$	33/2	−10.098	2.6560	−1.2862	0.8180	−0.6160	0.5260	−1/2	
$N = 15$	57/3	−11.314	2.7611	−1.1708	0.6058	−1/3	0.1708	−0.0528	
$N = 16$	43/2	−13.137	3.4142	−1.6199	1	0.7232	0.5858	−0.5198	1/2
$N = 17$	24	−14.557	3.5728	−1.5340	0.81413	−0.4732	0.2781	−0.1479	0.0465

Note. All devices have the same unit revival rate: $h\upsilon = 1$.

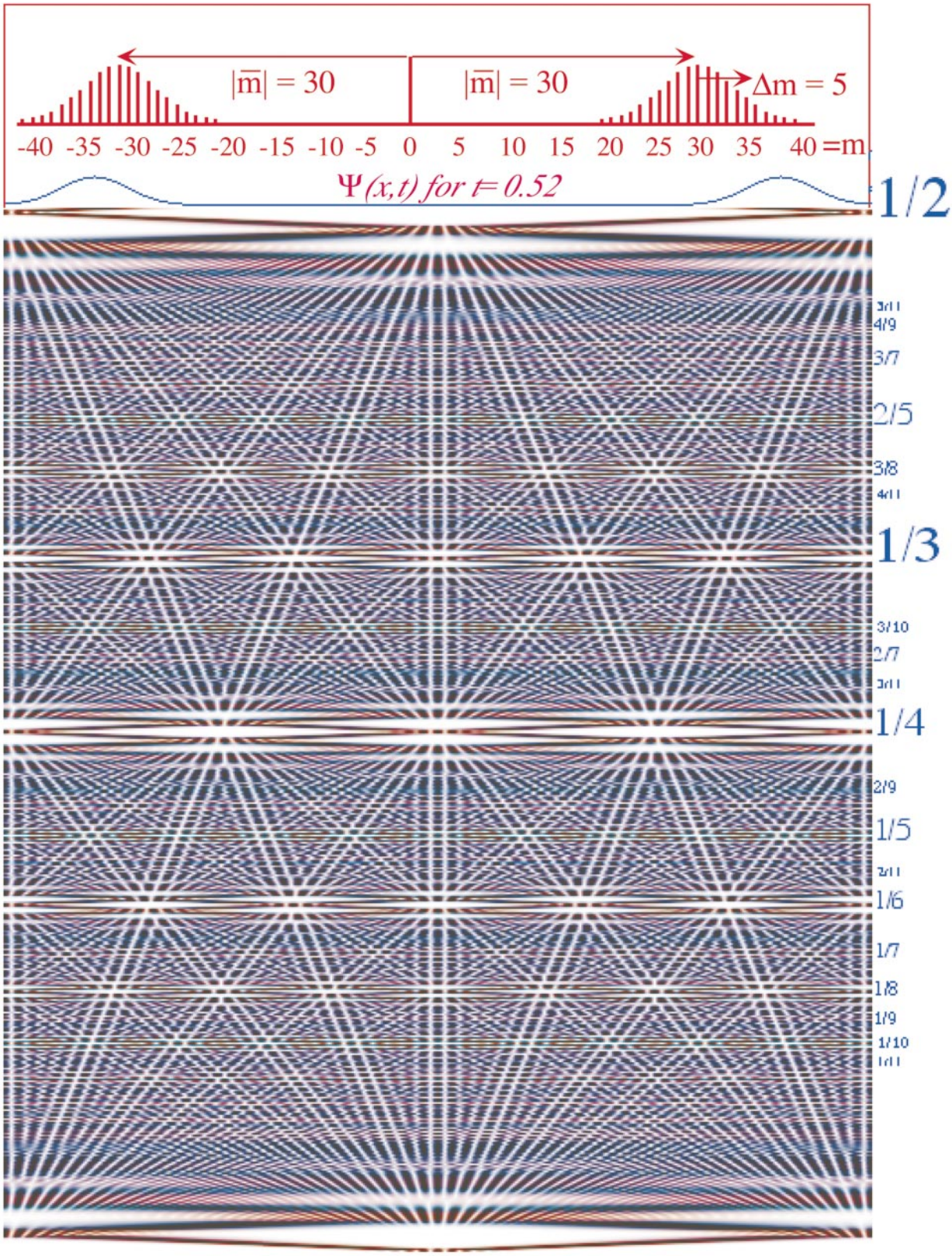

FIG. 11. Bimodal Gaussian distribution with $\bar{m} = 30$, $\Delta m = 5$ and $\Delta x = 0.04(2\pi)$. Quantum speed limit for spreading: $2\Delta m = 10$. Average packet speed: $\bar{m} = 30$.

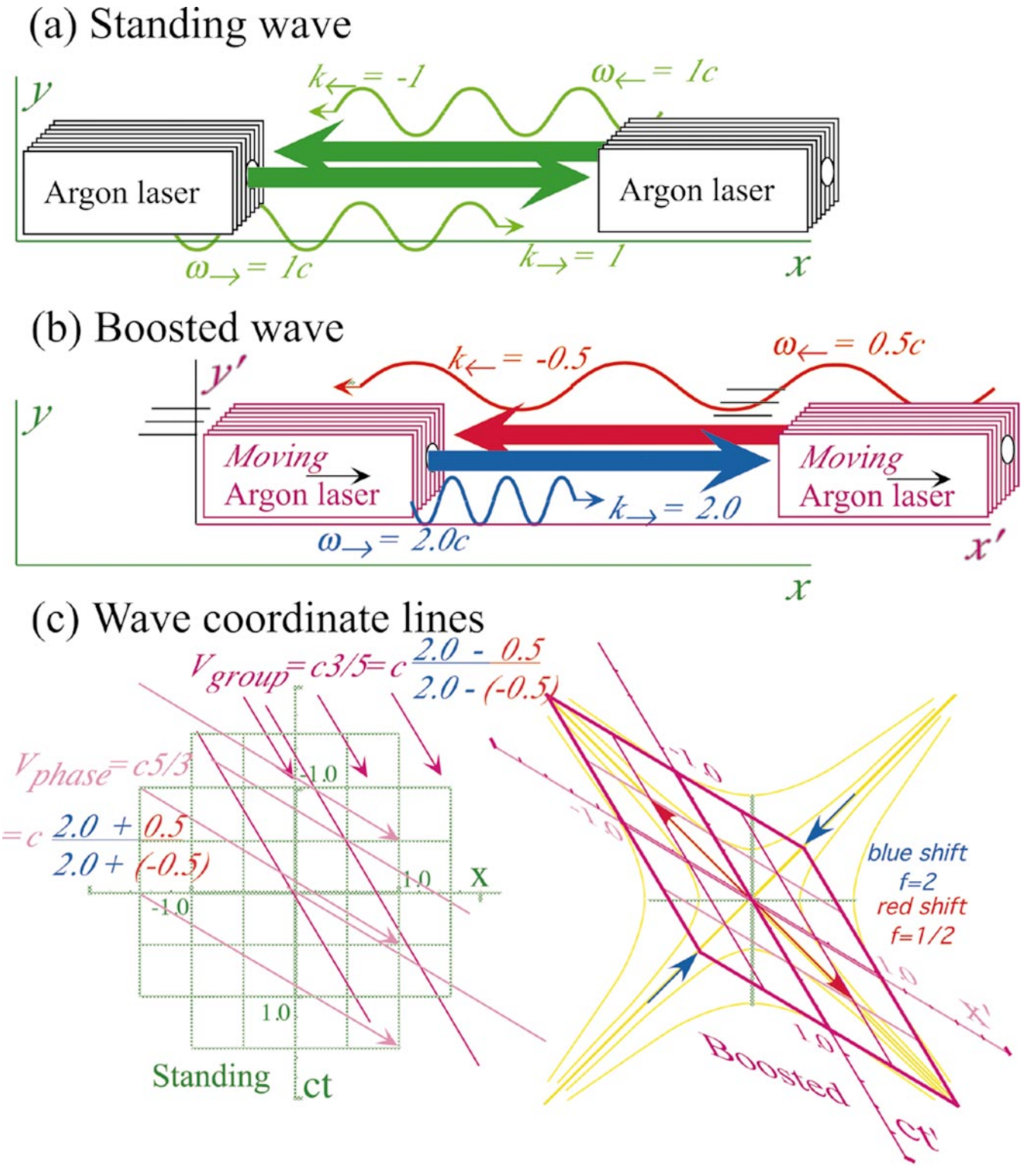

FIGURE A.1

standing wave space–time pattern. Boosting both lasers to the right at velocity u, or what is equivalent, boosting the observer to the left with velocity $-u$ gives a blue-shifted frequency $\omega_{\rightarrow} = f\omega_0$ from the left laser and a red-shifted frequency $\omega_{\leftarrow} = \omega_0/f$ from the right laser as in Fig. A.1b:

$$\omega_{\rightarrow} = f\omega_0 \quad \omega_{\leftarrow} = \omega_0/f. \tag{A.1a}$$

Wavevectors are likewise shifted in order to keep the phase speed c of light the same for all colors:

$$k_{\rightarrow} = fk_0 \quad k_{\leftarrow} = -k_0/f. \tag{A.1b}$$

This is a relativistic postulate: "throwing" light changes its color but not its speed c:

$$c = \omega_0/k_0 = \omega_{\rightarrow}/k_{\rightarrow} = -\omega_{\leftarrow}/k_{\leftarrow}. \tag{A.1c}$$

The right-hand laser emits to the left, and so its wavevector is negative. This yields the phase velocity indicated by "fast" trajectory lines in the space–time graphs of Fig. 1c and Fig. A.1c. A light phase speed $c = \omega_0/k_0$ is used:

$$V_{\text{phase}} = \frac{\omega_{\rightarrow} + \omega_{\leftarrow}}{k_{\rightarrow} + k_{\leftarrow}} = \frac{f + 1/f}{f - 1/f}\left(\frac{\omega_0}{k_0}\right) = \frac{f^2+1}{f^2-1}c. \tag{A.2}$$

The group velocity corresponds to "slow" trajectory lines in the space–time graphs of Fig. 1c and Fig. A.1c:

$$V_{\text{group}} = \frac{\omega_{\rightarrow} - \omega_{\leftarrow}}{k_{\rightarrow} - k_{\leftarrow}} = \frac{f - 1/f}{f + 1/f}\left(\frac{\omega_0}{k_0}\right) = \frac{f^2-1}{f^2+1}c = u. \tag{A.3}$$

Note that the standing-wave group envelope, stationary in the laser frame, moves at velocity u in the observer's frame. Solving (A.3) for the frequency shift factor f gives the well-known relativistic Doppler formula

$$f^2 = \frac{1 + u/c}{1 - u/c} = \frac{1+\beta}{1-\beta}, \quad f = \sqrt{\frac{1+\beta}{1-\beta}}. \tag{A.4}$$

The standard shorthand $\beta = u/c$ for the relativity parameter is used. Frequency shifts of $f = 2$ and $f = 1/2$ in Fig. A.1c correspond to $\beta = 3/5$ and $\beta = -3/5$, that is, relative separation or closure rates that are 60% of the speed of light.

The wave-zero space–time trajectories in Fig. A.1c are the images of a square standing-wave grid as seen by a moving observer. It is as though the lasers are optically "computing" a space–time grid for all possible observers by simply fixing a standing wave Ψ between them so Ψ-zeros draw their own Cartesian (x', ct')-grid:

$$\begin{aligned}\Psi_{\text{Standing}} = \Psi_{\text{Cartesian}} &= \frac{1}{2}e^{i(k_0x' - \omega_0t')} - \frac{1}{2}e^{i(-k_0x' - \omega_0t')} \\ &= ie^{-i\omega_0t'}\sin k_0x'.\end{aligned} \tag{A.5a}$$

This is a special case of Eq. [1] (repeated below) if the observer (x, ct)-frame is the same as the laser (x', ct')-frame, that is, there is no Doppler shift ($f = 1$). Otherwise, Ψ-zeros draw a Minkowski (x', ct')-grid of Fig. 1c or Fig. A.1c in the observer's (x, ct)-frame using zeros of the general Minkowski wave $\Psi_{\text{Minkowski}}$ given here:

$$\begin{aligned}\Psi_{\text{Minkowski}} &= \frac{1}{2}e^{i(k_{\rightarrow}x - \omega_{\rightarrow}t)} - \frac{1}{2}e^{i(k_{\leftarrow}x - \omega_{\leftarrow}t)} \\ &= ie^{i\frac{(k_{\rightarrow}+k_{\leftarrow})x - (\omega_{\rightarrow}+\omega_{\leftarrow})t}{2}} \\ &\quad \times \sin\frac{(k_{\rightarrow} - k_{\leftarrow})x - (\omega_{\rightarrow} - \omega_{\leftarrow})t}{2}.\end{aligned} \tag{A.5b}$$

The first standing wave zero of [A.5a] to the right of the origin in the laser frame has an x' value for which $k_0x' = \pi$. The observer sees this as a "slow" ($V_{\text{group}} = 3c/5$) group wave node moving so that the group phase in [A.5b] is π, too. This gives an equation for a line of constant x' parallel to the ct'-time-axis in the observer's (x, ct)-frame. Group zeros stand still in the laser (x', ct')-frame (SWR = 0) and track "resting" phase zeros:

$$k_0x' = \text{const.} = \frac{(k_{\rightarrow} - k_{\leftarrow})x - (\omega_{\rightarrow} - \omega_{\leftarrow})t}{2} = \pi. \tag{A.6a}$$

Space axis lines ($t' = \text{const.}$) are "fast" zeros ($V_{\text{phase}} = 5c/3$) of $\text{Re}\Psi_{\text{Minkowski}}$ where the $\text{Re}(ie^{i\text{phase}})$ is zero:

$$-\omega_0\,t' = -k_0\,ct' = \text{const.} = \frac{(k_{\rightarrow} + k_{\leftarrow})x - (\omega_{\rightarrow} + \omega_{\leftarrow})t}{2} = \pi. \tag{A.6b}$$

This gives an equation for a line of constant t' parallel to the laser's x'-space-axis in the observer's (x, ct) frame. Phase zeros go *infinitely* fast in the laser (x', ct')-frame ($1/\text{SWR} = \infty$). [A.6] holds for all values of (const.).

Using [A.1] with [A.4] in [A.6] gives the Einstein–Lorentz transformation equations [4] of special relativity. The result is immediately given in standard form with $\beta = u/c = \tanh\theta$ defining a hyperbolic angle θ:

$$\begin{aligned}x' &= \frac{(f + 1/f)x - (f - 1/f)(\omega_0/k_0)t}{2} \\ &= \frac{x - \beta\,ct}{\sqrt{1-\beta^2}} = x\cosh\theta - ct\sinh\theta\end{aligned} \tag{A.7a}$$

$$\begin{aligned}ct' &= \frac{-(f - 1/f)x + (f + 1/f)(\omega_0/k_0)t}{2} \\ &= \frac{-\beta x + ct}{\sqrt{1-\beta^2}} = -x\sinh\theta + ct\cosh\theta.\end{aligned} \tag{A.7b}$$

The laser's square (x, ct)-grid squares become (x', ct')-diamonds as the first quadrant diagonals stretch by the Doppler factor $f = 2$ and the second quadrant diagonals shrink by the

same factor. Thus, area of a given square is invariant to boost velocity u. Grid area invariance makes the points on the coordinate axes follow equilateral hyperbolas. This is more easily seen using coordinate axes ($v = x + ct,\ w = x - ct$) oriented along the $\pm 45^\circ$-diagonals. (These are *Finkelstein (21) coordinates*.) A rectangle defined by ($v = 0$, $w = B$), ($v = A$, $w = 0$), ($v = 0$, $w = 0$), and ($v = A$, $w = B$) maintains its area only if its corner ($v = A$, $w = B$) satisfies the following as velocity u varies:

$$vw = AB = \text{const.} = (x + ct)(x - ct) = (x)^2 - (ct)^2. \quad [A.8]$$

Note that the hyperbolas $(x)^2 - (ct)^2 = 0, \pm 1, \pm 2, \ldots$ plotted in Fig. A.1c are tangent to grid lines. This is an important feature of the geometry and kinematics of relativistic dispersion since tangents represent group velocity.

APPENDIX B

Wave-Based Derivation of Wavevector-Frequency Transformation

A key axiom for wave-based relativity theory is the demand for phase invariance. The main idea is that light waves themselves *are* suitable clocks for the Einstein theory. Each "tick" of a phase clock is a proper event; a particular reading on a wave phase clock that can be "stamped" so all observers must agree on it. In fact this is one of the principles behind the GPS or Global Positioning System.

For a plane wave $e^{i(kx-\omega t)}$, the phase is the argument of the exponential. In fact, its invariance equation

$$kx - \omega t = k'x' - \omega' t' \quad [B.1]$$

was used to derive the Lorentz relations [A.6] and [A.7]. Equation [B.1] is analogous to space–time invariant relations

$$x_1 x_2 - ct_1 ct_2 = x_1' x_2' - ct_1' ct_2' \quad [B.2a]$$

or the hyperbolic sections [A.8] of the light cone

$$(x)^2 - (ct)^2 = (x')^2 - (ct')^2, \quad [B.2b]$$

which follow from [A.7]. Equations [B.1] and [B.2] are related to the constancy of the speed of light ($c = \omega/k = \omega'/k'$). Finally, invariance of $kx - \omega t = kx - (\omega/c)(ct)$ implies that wavevector–frequency variables $(k, \omega/c)$ or (kc, ω) must Lorentz transform just like space–time variables (x, ct) or $(x/c, t)$; that is, in analogy to [A.7] one has

$$ck' = \frac{ck - \beta\omega}{\sqrt{1-\beta^2}} = ck\cosh\theta - \omega\sinh\theta \quad [B.3a]$$

and

$$\omega' = \frac{-\beta\, ck + \omega}{\sqrt{1-\beta^2}} = -ck\sinh\theta + \omega\cosh\theta. \quad [B.3b]$$

This implies the (kc, ω) pair have their own hyperbolic invariant (see Fig. 2a),

$$(kc)^2 - (\omega)^2 = (k'c)^2 - (\omega')^2 = -\mu^2 = \text{const.} \quad [B.4]$$

For light, [B.4] is a trivial result of c-constancy ($c = \omega/k = \omega'/k'$). (The invariant constant μ is zero for a light cone.) However, the phase invariance axiom [B.1] applies to more than electromagnetic waves, as described below.

APPENDIX C

Wave-Based Derivation of Relativistic Quantum Kinematics

Relativistic symmetry requires that phase invariance [B.1] and relations [B.3] through [B.4] apply to matter waves as well as light waves. For matter, however, the hyperbolic invariant [B.4] is nonzero; that is, it will be a nondegenerate hyperbola in (kc, ω)-space:

$$(\omega)^2 - (kc)^2 = (\omega')^2 - (k'c)^2 = \mu^2 > 0. \quad [C.1]$$

For each matter wave there exists a frame in which the wavevector k is zero; that is, $(k'c, \omega') = (k_0 c, \omega_0) = (0, \mu)$. This is called the *rest-frame* of the matter or "particle." The invariant constant $\mu = \omega_0$ turns out to be related to the rest mass, inertia, and rest energy of a particle, three quite distinct physical quantities.

Inverting [B.3] shows how such a "rest wave" ($(k'c, \omega') = (0, \mu)$) appears if boosted to velocity $u = \beta c$:

$$ck = \frac{ck' + \beta\omega'}{\sqrt{1-\beta^2}} = \frac{0 + \mu u/c}{\sqrt{1-(u/c)^2}} = \mu\frac{u}{c} - \frac{1}{2}\mu\left(\frac{u}{c}\right)^3 \quad [C.2a]$$

$$\omega = \frac{\beta ck' + \omega'}{\sqrt{1-\beta^2}} = \frac{0 + \mu}{\sqrt{1-(u/c)^2}} = \mu + \frac{1}{2}\mu\left(\frac{u}{c}\right)^2 + \cdots. \quad [C.2b]$$

Planck's axiom supposes the equivalence of energy and frequency ($E = \hbar\omega$). This is applied to [C.2b]:

$$E = \hbar\omega = \hbar\mu + \frac{1}{2}\hbar\mu\left(\frac{u}{c}\right)^2 + \cdots. \quad [C.3]$$

Applying the invariant constant μ to the Einstein rest energy–frequency $Mc^2/\hbar$ leads to a familiar $\frac{1}{2}Mu^2$ variation for Newtonian particle energy for subrelativistic particle velocity

$u \ll c$. Added to this is a constant *rest energy* Mc^2:

$$E = \hbar\omega = Mc^2 + \frac{1}{2}Mu^2 + \cdots. \qquad [C.4]$$

Setting $\mu = Mc^2/\hbar$ in the k-expression [C.2a] yields Galilean–Newtonian momentum $p = Mu$ to first order in u/c:

$$\hbar k = Mu + \frac{1}{2}Mc^2\left(\frac{u}{c}\right)^3 + \cdots. \qquad [C.5]$$

This completes the Einstein–DeBroglie formula for the relativistic quantum particle momentum–wavevector:

$$p = \hbar k = \frac{Mu}{\sqrt{1-(u/c)^2}}. \qquad [C.6a]$$

The Einstein–Planck energy formula for relativistic energy–frequency follows, too:

$$E = \hbar\omega = \frac{Mc^2}{\sqrt{1-(u/c)^2}}. \qquad [C.6b]$$

The momentum equation [C.6a] and energy equation [C.6b] are solved for the boost or group velocity u:

$$\frac{u}{c} = \frac{\sqrt{E^2-(Mc^2)^2}}{E} = \frac{cp}{E} = \frac{cp}{\sqrt{(Mc^2)^2+(cp)^2}}. \qquad [C.7]$$

The preceding uses the energy–momentum invariant derived from Eq. [C.1] or [B.4]:

$$E^2 - (cp)^2 = (Mc^2)^2 = \mu^2\hbar^2 \qquad [C.8a]$$

$$E = \hbar\omega = \sqrt{(Mc^2)^2+(cp)^2} = \sqrt{(Mc^2)^2+(c\hbar k)^2}. \qquad [C.8b]$$

The latter equation is the universal *dispersion function* $\omega(k)$ which determines phase and group velocities:

$$V_{\text{phase}} = \frac{\omega}{k} = \frac{E}{p} = \frac{c^2}{u} \qquad [C.9a]$$

$$V_{\text{group}} = \frac{d\omega}{dk} = \frac{dE}{dp} = \frac{c^2 p}{E} = u. \qquad [C.9b]$$

Nonrelativistic approximations of energy, such as [C.4] or Fig. 2b, may leave out the Mc^2 term since neither absolute energy nor absolute phase is physically observable. Only energy *difference* is physically important for classical mechanics, and only *relative* phase and phase velocity are observed in quantum mechanics. Neglecting a constant term such as Mc^2 in energy expression [C.4] does not change the group velocity $d\omega/dk = u$ or any observable wave behavior given by the probability envelope $\Psi * \Psi$ Eq. [1]. The $\Psi * \Psi$-envelope always has group velocity u according to Eqs. [3] and [6a]. (Recall Fig. 1c.) On the other hand, phase velocity ω/k is reduced by neglecting Mc^2 and changes from an enormous value c^2/u to a value of $u/2$ that is quite small in the nonrelativistic limit $u \ll c$; indeed, it becomes smaller by roughly half the group velocity. This, however, is consistent with classical physics or with experiments based on observing $\Psi * \Psi$ since the phase of Eq. [1] cancels out of $\Psi * \Psi$, and so absolute phase velocity is not observable.

Classical mechanics is concerned only with particle velocity u and momentum p, which are *directly* proportional to the wave group velocity. (Relativistic phase velocity c^2/u is *inversely* proportional to group velocity u.) The rate of change ($dp/dt = \hbar\, dk/dt$) of momentum is proportional to applied force in quantum as well as classical dynamics. The proportionality constant is called *effective mass* M_{eff} or local inertia:

$$M_{\text{eff}} = \frac{F}{a} = \frac{\hbar\frac{dk}{dt}}{\left(\frac{dV_{\text{group}}}{dt}\right)} = \frac{\hbar\frac{dk}{dt}}{\left(\frac{dV_{\text{group}}}{dk}\frac{dk}{dt}\right)}$$
$$= \frac{\hbar}{\left(\frac{d^2\omega}{dk^2}\right)} = \frac{1}{\left(\frac{d^2E}{dp^2}\right)} = \frac{M}{(1-\beta^2)^{3/2}}. \qquad [C.10]$$

So effective mass is inversely proportional to the *curvature* of the dispersion function. This result may seem paradoxical in light of the observation that a photon dispersion function is a straight line ($\omega = c|k|$), so its effective mass would seem to be infinite. But photon group and phase velocity never change no matter how large the "force" is, and so the photon's effective mass is indeed infinite. Furthermore, as an electron or any other particle nears the speed of light, its effective mass also approaches infinity.

What we call the mass M of a particle is really its *rest mass*, that is, its effective mass at zero wavevector ($k = 0$). The photon dispersion function ($\omega = c|k|$) has a kink with infinite curvature at the origin, so its rest mass, according to Eq. [C.11], is indeed zero. Physically, a ($k = 0$)–photon corresponds to a uniform static electric field. However, the very slightest boost of such a system will suddenly result in a finite wavevector with speed c. This behavior is consistent with a zero mass and infinite acceleration for the electric rest-wave as it becomes a normal light wave. After the tiny boost the light wave has infinite inertia and zero acceleration, as usual.

REFERENCES AND NOTES

1. J. H. Eberly, *Phys. Rev. A* **23,** 236–245 (1981).
2. The first computer movie recording perfect fractional revivals may have been one done at Los Alamos in 1982 using molecular rotational wavepackets. Since it ran way over budget, only one was made. R. S. McDowell, W. G. Harter, C. W. Patterson, *Los Alamos Science* **3**(1), 38–65 (1982).
3. S. I. Vetchinkin, A. S. Vetchinkin, V. V. Eryomin, and I. M. Umanskii, *Chem. Phys. Lett.* **215,** 11–14 (1993).
4. D. L. Aronstein and C. R. Stroud Jr., *Phys. Rev. A* **55,** 4526–4536 (1997); C. R. Stroud Jr. and M. Noel, *Opt. Photon. News* **10,** 35–37 (1999).

5. W. Kinzel, *Phys. BI* **51,** 1190–1199 (1995).
6. I. S. Averbukh and N. F. Perelman, *Phys. Lett.* **139,** 449–453 (1989).
7. M. V. Berry, *J. Phys. A Math. Gen.* **29,** 6617–6629 (1996).
8. F. Grosmann, J. M. Rost, and W. P. Schleich, *J. Phys. A Math. Gen.* **30,** L277–283 (1997).
9. A. E. Kaplan, P. Stifter, K. A. H. vanLeeuwen, W. E. Lamb Jr., and W. P. Schleich, *Phys. Scr.* **76,** 93–97 (1998). M. J. W. Hall, M. S. Reineker, and W. P. Schleich, *J. Phys. A Math. Gen.* **32,** 8275–8291 (1999).
10. W. G. Harter, *et al., Am. J. Phys.* **53**(7), 671–679 (1985); *Comput. Phys.* **5,** 466–478 (Sept. 1991).
11. R. P. Feynman, R. B. Leighton, and M. Sands, "The Feynman Lectures on Physics," Vol. 3, 7–4. Addison-Wesley, Reading, MA, 1964.
12. D. R. Hofstadter, *Phys. Rev. B* **14,** 6 (1976); "Godel, Escher, Bach: An Eternal Golden Braid," pp. 144–145. Vintage–Random House, New York, 1989.
13. S. Ostlan and S. Kim, *Phys. Scr.* **9,** 193–198 (1985).
14. John Farey, *Philos. Mag.* **47,** 385–390 (1816).
15. H. G. Schuster, *in* "Deterministic Chaos," pp. 159–160. VCH, Weinheim, 1989.
16. P. Cvitanovic, *in* "From Number Theory to Physics," (M. Waldschmidt, P. Mousa, J.-M. Luck, and C. Itzykson, Eds.), Chap. 13. Springer-Verlag, Berlin, 1990.
17. W. G. Harter, "Principles of Symmetry, Dynamics, and Spectroscopy," pp. 89–94. Wiley, New York 1993.
18. W. G. Harter, *Phys. Rev. A* **64,** 012312-1-17 (2001).
19. H. Caspar, *et al., Science* **290,** 773–777 (2000).
20. Nonrelativistic particle waves share with hydrodynamic gravity waves a ratio of 1 : 2 between group and phase velocities. The difference is that, for gravity waves, the group velocity is half, not twice, the phase velocity.
21. D. Finkelstein, *Phys. Rev.* **110,** 965–967 (1958).